appliedoptics

Photoacoustic imaging of lamina cribrosa microcapillaries in porcine eyes

Thanadet Chuangsuwanich,[1,†] Mohesh Moothanchery,[2,†] Alvan Tsz Chung Yan,[1] Leopold Schmetterer,[3,4,5,6,7] Michaël J. A. Girard,[1,4,8] and Manojit Pramanik[2,*]

[1]*Ophthalmic Engineering & Innovation Laboratory, Department of Biomedical Engineering, National University of Singapore, Singapore, Singapore*
[2]*School of Chemical and Biomedical Engineering, Nanyang Technological University, 62 Nanyang Drive, 637459 Singapore, Singapore*
[3]*Lee Kong Chian School of Medicine, Nanyang Technological University, 59 Nanyang Drive, 637459 Singapore, Singapore*
[4]*Singapore Eye Research Institute, Singapore National Eye Centre, Singapore, Singapore*
[5]*Visual Science Academic Clinical Programme, Duke-NUS, Singapore, Singapore*
[6]*Department of Clinical Pharmacology, Medical University of Vienna, Vienna, Austria*
[7]*Center of Medical Physics and Biomedical Engineering, Medical University of Vienna, Vienna, Austria*
[8]*e-mail: mgirard@nus.edu.sg*
Corresponding author: manojit@ntu.edu.sg

Due to the embedded nature of the lamina cribrosa (LC) microcapillary network, conventional imaging techniques have failed to obtain the high-resolution images needed to assess the perfusion state of the LC. In this study, both optical resolution (OR) and acoustic resolution (AR) photoacoustic microscopy (PAM) techniques were used to obtain static and dynamic information about LC perfusion in *ex vivo* porcine eyes. The OR-PAM system could resolve a perfused LC microcapillary network with a lateral resolution of 4.2 μm and also provided good depth information (33 μm axial resolution) to visualize through-thickness vascular variations. The AR-PAM system was capable of detecting time-dependent perfusion variations. This study represents the first step towards using an emerging imaging modality (PAM) to study the LC's perfusion, which could be a basis for further investigation of the hemodynamic aspects of glaucomatous optic neuropathy.   © 2018 Optical Society of America

OCIS codes: (170.5120) Photoacoustic imaging; (330.4460) Ophthalmic optics and devices; (170.2655) Functional monitoring and imaging.

https://doi.org/10.1364/AO.57.004865

1. INTRODUCTION

Open angle glaucoma (OAG) is an optic neuropathy disease characterized by a progressive loss of retinal ganglion cells (RGCs). The disease appears to start within the optic nerve head (ONH), where RGC axons are damaged, potentially due to mechanical stress and other unidentified mechanisms. The primary risk factor for OAG is an elevated intraocular pressure (IOP); however, the causal link between elevated IOP and RGC loss has yet to be established—up to a third of OAG patients do not have elevated IOP, and not all individuals with significantly elevated IOP develop glaucoma [1]. It has been speculated that several loads (IOP, the cerebrospinal fluid pressure [2], and optic nerve traction forces [3]) can cause RGC axonal death by inducing biomechanical insult to the ONH tissue, causing direct mechanical damage to the RGC and disrupting axonal transport of essential trophic factors [4–6]. Another possible pathway for RGC damage relates to the vascular deficiency—alterations in the structures of the ONH due to a modified biomechanical environment or poor ocular

hemodynamics could predispose a person to ischemic RGC death [7–10].

To date, both mechanical and vascular factors have been assumed to be involved in glaucoma pathogenesis, but the exact relationship between these factors remains unclear. This is partially due to limitations of current imaging modalities that are unable to visualize the complex 3D microcapillary network of the lamina cribrosa (LC). The LC is a sieve-like structure located deep within the ONH and is thought to be the major site of RGC damage within the ONH. The LC consists of collagenous connective tissues that provide structural support to the ONH; the LC also provides nutrients and oxygen to the RGC axons via the microcapillaries that are embedded within the collagenous beams [11]. Studying the hemodynamics of LC microcapillaries could be the key to understanding the mechanisms behind RGCs' death. Unfortunately, the LC's deep location and the embedment of the microcapillaries severely limit the ability of standard optical imaging modalities (e.g., optical coherence tomography, multiphoton microscopy, and confocal

microscopy) to maintain sufficient penetration depth and spatial resolution to resolve the LC microcapillaries both *ex vivo* and *in vivo* [12].

Photoacoustic (PA) imaging is an emerging modality that has several advantages over conventional optical modalities in imaging embedded biological structures [13–16]. By combining optics with ultrasound, PA imaging can provide a penetration depth beyond the optical mean free path (~1 mm in tissue) with high resolution. PA imaging has been successfully applied to *in vivo* structural, functional, and molecular imaging [17–20]. In photoacoustic imaging, a short laser pulse irradiates the natural chromophores in the tissue, inducing heat and the emission of detectable acoustic waves [known as photoacoustic (PA) waves] from the tissue. Acoustic resolution photoacoustic microscopy (AR-PAM) utilizes weak optical and tight acoustic focusing and can achieve deep tissue imaging, with an imaging depth greater than 3 mm and a lateral resolution of 45 µm [21–24]. Optical resolution photoacoustic microscopy (OR-PAM) utilizes tight optical focusing to achieve a lateral resolution of up to 0.5 µm, with a penetration depth of 1.4 mm [25–27]. Photoacoustic imaging has been applied for eye imaging earlier [19,28–31]. Jeon, *et al.* [32] has recently shown that PA imaging is capable of resolving and retaining the depth information of anterior choroidal vasculature in mice; however, no studies have imaged the optic nerve head blood flow and the LC in detail using PA imaging modalities.

In this study, we aimed to image LC microcapillaries using a switchable AR- and OR-PAM (AR-OR-PAM) imaging system capable of both high-resolution imaging as well as low-resolution deep tissue imaging utilizing the same laser and scanner [21]. OR-PAM was used to obtain high-resolution images of perfused porcine LCs with a lateral resolution of 4.2 µm. AR-PAM was used to image the intact eye from the posterior of the ocular globe and conduct a time-dependent *ex vivo* perfusion study. This is the first study to image the LC microcapillaries in detail using photoacoustic imaging, and it can be a basis for further studies to elucidate the role of blood flow in glaucoma disease.

2. MATERIALS AND METHODS

A. Porcine Eye Preparation and Perfusion

Fresh porcine eyes (within 24 h post-mortem) were obtained from a local abattoir (Jurong Abattoir, Singapore). Eyes were enucleated by the abattoir with at least 1 cm of optic nerve intact and extraorbital tissues preserved. A routine removal of muscles and fats was performed, with special care to avoid damaging the scleral shell, the ciliary arteries, and the vortex veins. The eyes were then cleansed briefly in a 1× phosphate-buffered saline (PBS) solution before perfusion.

To perfuse the LC, two long posterior ciliary arteries (one of each opposite side of the globe) were cannulated carefully with 27G needles under a light microscope (Zoom Stereo Microscope, Amscope, Singapore), ensuring that the needles did not penetrate the sclera (Fig. 1). A syringe pump (KDS100L, KD Scientific, Singapore) with a 50 mL Terumo syringe was used to drive the flow through a Tygon Microbore Autoanalysis tube (1.27 mm inner diameter); the tube was bifurcated via a *Y*-shape connector to the two 27G needles
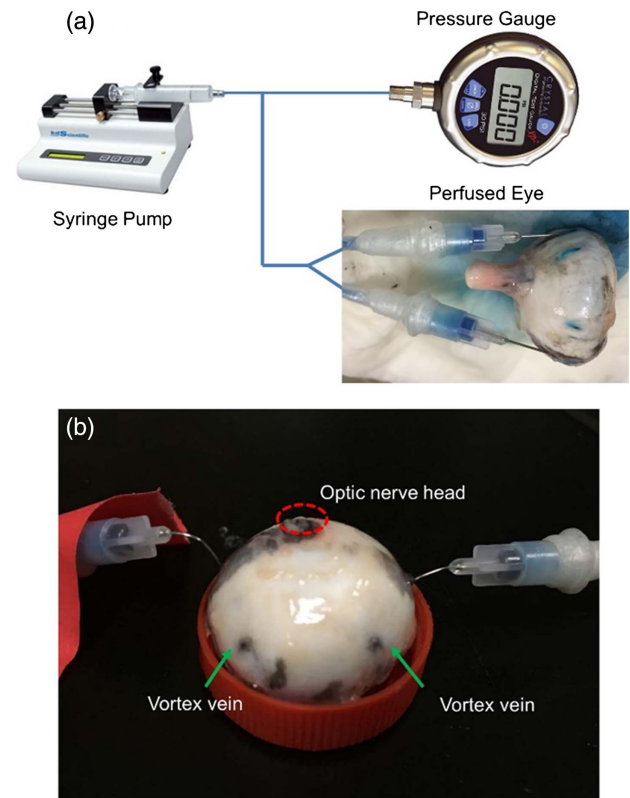

Fig. 1. (a) Schematic of a perfusion system, consisting of a variable syringe pump (with 50 mL Terumo syringe), 1.27 mm Tygon Microbore Autoanalysis tube, a digital test gauge, and two 27G needles cannulated to the ciliary arteries. (b) Modified setup for AR-PAM imaging. Red dotted-circle is the region of interest (ONH); green arrows point to the vortex veins.

[Fig. 1(a)]. Perfusion pressure was measured continuously with a pressure gauge (15 Psi XP2i Digital Pressure Gauge, Crystal Engineering, USA). Two contrast agents were employed for this experiment: (1) either an artificial blue color dye (E133) with four drops of dye used per 50 mL of water (~6 mM); or (2) a medical-grade activated carbon dissolved in water (1 mg/mL). Perfusion was done with a constant flow rate of 4 mL/min; this rate was deduced from numerous trials to obtain a stable perfusion pressure and a constant outflow from the vortex vein. The perfusion time was at least 30 min for each successful perfusion. Note that for simplicity, IOP was not measured nor controlled in this experiment.

For OR-PAM imaging, the eyes were perfused for 30 min and the ONHs were immediately trephined (1 cm in diameter including the peripapillary sclera and the LC in its center; intraorbital tissues were preserved), to allow OR-PAM scanning from the anterior of the LCs. This was necessary as the current OR-PAM system's working distance (6.7 mm) did not allow for imaging of the LC from outside the ocular globe. Both contrast agents were used for OR-PAM imaging.

For time-dependent flow imaging using AR-PAM, the eye's cornea was fixated on a small plastic cup using cyanoacrylates [Fig. 1(b)]. The arteries were cannulated with curved 27G needles to make room for the acoustic probe [Fig. 1(b)]. AR-PAM

imaging was performed from the posterior of the ocular globe during perfusion. Dissolved activated carbon was the sole contrast agent for AR-PAM imaging.

B. Photoacoustic Microscopy System

The schematic of the switchable OR-AR-PAM is shown in Fig. 2 and was previously described in detail [33]. Briefly, the OR-AR-PAM system employs a nanosecond tunable laser system, consisting of a diode-pumped solid-state Nd-YAG laser (INNOSLAB, Edgewave, Wurselen, Germany) and a dye laser (Credo-DYE-N, Sirah dye laser, Spectra Physics, Santa Clara, California, USA). For the OR-PAM setup, the laser beam was spatially filtered and coupled on to a single-mode fiber (SMF; P1-460B-FC-1, Thorlabs). The output beam from the fiber was then collimated using an achromatic doublet L2 (32-317, Edmund Optics), reflected by a stationary elliptical mirror M, and filled the back aperture of another identical achromatic lens L3. The beam then passed through an optoacoustic beam combiner consisting of a right-angled prism (RA) and a rhomboid prism (RP) with a layer of silicon oil (SO) in between. An acoustic lens (AL; LC4573, Thorlabs) providing acoustic focusing (focal diameter ~46 μm) was attached to the bottom of the rhomboid prism. A 50 MHz ultrasonic transducer (UST; V214-BB-RM, Olympus-NDT) was placed on top of the rhomboid. To maximize the detection sensitivity, the optical and acoustic foci were aligned confocally. The laser repetition rate for the OR-PAM was set to 5 kHz, and the laser energy at focus could be varied up to 200 nJ per pulse.

For AR-PAM scanning, the laser beam was diverted using a right-angle prism (RAP), placed on a computer-controlled motorized stage and coupled onto a multimode fiber (MMF; M29L01, Thorlabs). The beam out from the fiber was collimated using lens L1 (LA1951, Thorlabs) and then passed through a conical lens Con.L (1-APX-2-B254, Altechna) to provide a ring-shaped beam. The ring-shaped beam was allowed to focus weakly onto the specimen with the focal region coaxially overlapping the ultrasonic focus inside the tissue using a homemade optical condenser having a 50 MHz ultrasonic

transducer in the center (V214-BB-RM, Olympus-NDT). An acoustic lens, (AL; LC4573, Thorlabs) was attached to the bottom of the transducer. The laser repetition rate (LRR) was set to be 1 kHz, and the laser energy at focus could be varied up to 40 μJ per pulse. The optical illumination on the object surface was donut shaped with a dark center so that no strong photoacoustic signals were produced from the surface on the object within the ultrasonic field of view.

The OR-PAM system had a lateral resolution of 4.2 μm and an axial resolution of 33 μm as demonstrated earlier [21]. To complete each scan for the LC and peripapillary region covering the area of approximately 3 mm × 3 mm, the OR-PAM system took ~30 min, capturing 1500 B-scans in total with 1500 A-scans per B-scan. The AR-PAM system had a lateral resolution of 45 μm and an axial resolution of 33 μm [21]. To complete the scans for the LC and peripapillary region (3 mm × 3 mm), the AR-PAM system took ~4 min, capturing 200 B-scans in total with 200 A-scans per B-scan.

The OR-AR-PAM scanner head was attached to a three-axis motorized stage using a homemade switchable plate. For photoacoustic imaging, the bottom of the OR-AR-PAM scanner head was submerged in a water-filled tank with an imaging window opened and sealed with a polyethylene membrane at the bottom of the tank for optical and acoustic transmission. The scanning and data acquisition was controlled using LabVIEW software. The synchronization of the data acquisition and the stage motion were controlled through the signal from a photodiode (PD). A beam sampler (BS) was placed in front of the laser beam to divert a small portion of the beam (5%) to the PD. Two-dimensional continuous raster scanning of the imaging head was used during image acquisition.

C. Post-Processing of the Photoacoustic Microscopy Images

Maximum amplitude projection (MAP) of photoacoustic microscopy images (both AR-PAM and OR-PAM) was generated using MATLAB (Matlab 2014b, The Mathworks Inc., Natic, Massachusetts). MAP image is obtained by projecting the maximum photoacoustic amplitude along the depth direction (z axis) to its orthogonal plane ($x – y$ plane parallel to the LC surface). It is very similar to maximum intensity projection (MIP) used in visualization of 3D volumetric imaging data in other modalities. Instead of maximum intensity, here we use the maximum amplitude of the PA signals. The LC border was manually marked for the image segmentation algorithm (MATLAB) to isolate the LC's signal in the OR-PAM images. Analysis of signal intensity within regions of interest of the AR-PAM scans and their respective statistical analyses were also performed in MATLAB.

Fig. 2. Schematic of the AR-OR-PAM system. BS, beam sampler; NDF, neutral density filter; RAP, right-angle prism; PD, photodiode; CL, condenser lens; PH, pinhole; FC, fiber coupler; UST, ultrasound transducer; MMF, multimode fiber; SMF, single-mode fiber; DAQ, data acquisition card; TS, translation stage; Con.L, conical lens; L1, convex lens; L2 and L3, achromatic lens; RA, right-angle prism; RP, rhomboid prism; OC, optical condenser; M, mirror; SP, slip plate; LT, lens tube; AL, acoustic lens; and SO, silicon oil.

3. RESULTS

A. Imaging of Perfused and Non-Perfused LCs Using OR-PAM

High-resolution images (OR-PAM has a lateral resolution of 4.2 μm) of trephined LCs were obtained using OR-PAM. For the control LC (without prior perfusion), no signal was observed from the LC itself, but the surrounding area, marked by the scleral canal wall, exhibited a strong signal [Fig. 3(a)].
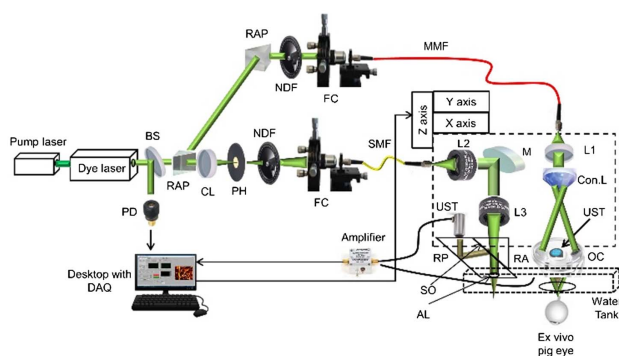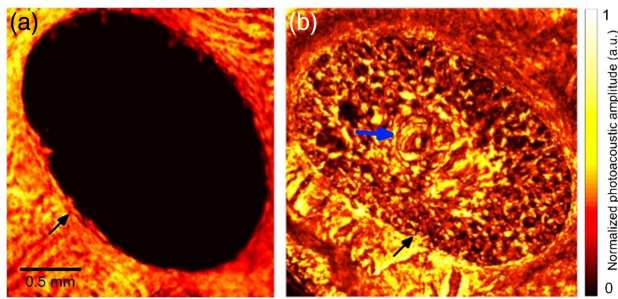
Fig. 3. OR-PAM images (maximum amplitude projection) of perfused and non-perfused LC. (a) An image of a non-perfused LC. (b) An image of a perfused LC with blue dye as a contrast agent. Black arrow points to the border between LC and the sclera (scleral canal opening). Blue arrow points to the ventral opening of the LC. All PAM MAP images have a lateral resolution of 4.2 µm.

In the eyes that were perfused with a blue dye solution, a strong signal from the LC was observed, revealing a mesh-like capillary network and some determining features, such as the ventral opening [Fig. 3(b)].

B. Perfusion Profile Along the LC's Depth from the OR-PAM Scan

Image segmentation is performed to mark the area of the lamina cribrosa [inside the blue border in Fig. 4(a)] from the surrounding scleral tissue. For each B-scan [Fig. 4(b)], the borders of the lamina cribrosa (arrowed) are digitally marked according to the border defined in Fig. 4(a). Signal from scleral tissue was removed from the original B-scans [Fig. 4(c)] to obtain B-scans with only signal from the LC [Fig. 4(d)]. The LC's signal intensity profile along its depth was then plotted [Fig. 4(e)]. It was observed that the depth of the LC was approximately 220 µm and the intensity profile peaked between the depths of 90 to 120 µm.
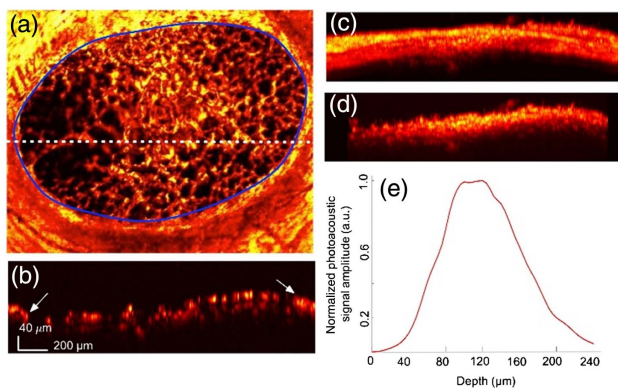

Fig. 4. OR-PAM B-scan and MAP images projected along the thickness of the LC. (a) MAP image of a perfused LC (carbon suspension) with blue line highlighting the scleral canal border. (b) A single B-scan along the white dotted line in (a) with lateral resolution of 4.2 µm and axial resolution of 33 µm. White arrows point to the scleral canal border. (c) MAP image projected along the thickness of the LC before segmentation. (d) MAP image after segmentation is done to isolate signal from the LC. (e) Intensity profile of the MAP image in (d) plotted along the depth of the LC.

C. Time-Dependent Imaging of LC Perfusion Using AR-PAM

Using AR-PAM, images at various time points for a continuous perfusion of an eye with carbon suspension were obtained (perfusion was stopped after 20 min). No image was acquired at $t = 0$ min (at the start of perfusion), as the eye was required to be pre-perfused to locate the area of the lamina cribrosa and to determine the correct focal length to be used. Both the scan area and focal length were then kept constant for all acquisitions. The first image acquired was at $t = 5$ min after the start of perfusion. It was observed that the signal intensity peaked at 20 min after perfusion [Fig. 5(a)] before decreasing significantly after the perfusion was stopped for 10 min ($t = 30$ min). The box-plot in Fig. 5(b) shows the mean photoacoustic signal intensity value calculated from a region of interest (dotted white box) with an area of 46×85 pixel. The mean photoacoustic signal intensity value (in volts) for each time point was: $t = 5$ min: 0.65 ± 0.15, $t = 10$ min: 0.60 ± 0.14, $t = 15$ min: 0.70 ± 0.17, $t = 20$ min: 0.81 ± 0.16, $t = 30$ min: 0.59 ± 0.17. Based on one-way ANOVA and post-hoc (pairwise t-test with Bonforroni correction) analysis, the mean intensity value at $t = 20$ min was significantly
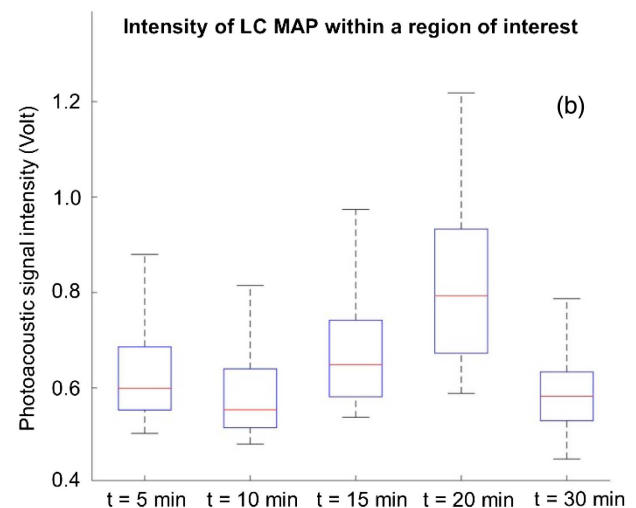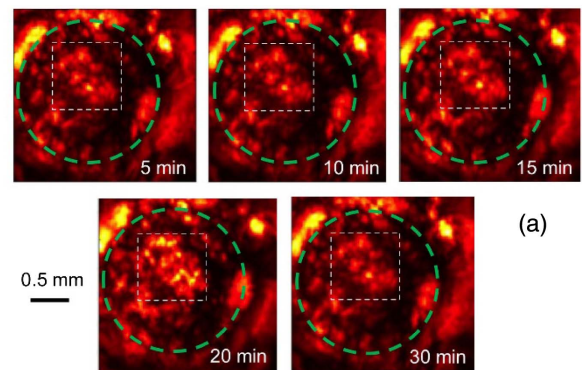

Fig. 5. Real-time perfusion images obtained from AR-PAM. (a) Images obtained at various time after the start of perfusion (perfusion is stopped at $t = 20$ min). Green dotted circles mark the ONH and LC region. (b) A box-plot of top 60% pixels with highest signal intensity in each region of interest [white dotted box in (a)]. Outliers are not shown.

higher than both the value at $t = 5$ min ($p < 0.05$) and $t = 30$ min ($p < 0.05$).

4. DISCUSSION

In this work, the capabilities of both the AR- and OR-PAM systems in imaging the LC microcapillaries were demonstrated. This is the first study that attempts to take photoacoustic image of the perfused LC microcapillaries, a structure which could be of critical importance in glaucoma. The results provided preliminary information on both the static and dynamic state of LC perfusion.

High-resolution images of the perfused LC from OR-PAM revealed mesh-like networks of microcapillaries [Figs. 3(b) and 4(a)], which were similar to the morphology of porcine LC collagenous beams observed from micro-computed tomography [34]. The similarity of LC microcapillaries and LC beams' morphology may prove that each LC beam contains a microcapillary, validating an important assumption used in computational hemodynamics study of the LC [7].

Both the contrast agents used (blue dye and activated carbon) in OR-PAM imaging readily absorbed the excitation laser (570 nm) and provided strong PA signals. When the eye was not perfused, there was no photoacoustic signal generated from the LC [Fig. 3(a)], and this acted as the negative control to validate that the observed LC's signals were originated from the contrast agents in the microcapillaries. Note that in both perfused and non-perfused (control) LCs, a strong signal could still be observed in Fig. 3 from region outside the ONH (marked by the scleral border), since the inner sclera is covered by a dark melanin from the retinal endothelium [35]. It should also be noted that the structures we observed in the LC region were likely to represent both the LC's collagen beams and the microcapillaries embedded inside. A dye-based contrast agent may diffuse out of the capillaries to partially stain the collagen beams, resulting in beams that look larger [Fig. 3(b)] when compared to an image resulting from a particulate contrast agent (carbon), which was less likely to diffuse out of the microcapillaries [Fig. 4(a)].

Image segmentation was also performed to isolate LC signals from the surrounding scleral tissue's signal. The segmented B-scans were then combined and projected on the depth-axis [Fig. 4(d)] of the LC to study the variation of perfusion level along the LC depth. This aspect is important as the LC's morphology is also heterogeneous along its depth, and this could have an impact on its blood flow [36,37]. It was also evident from a B-scan in Fig. 4(b) that there were multiple layers of signals emitting from the same axial scan, indicating the presence of multi-layered microcapillaries in the LC. From the analysis, the LC was approximately 220 μm thick, which was close to the reported value in porcine eyes (200 μm ± 32 μm) [38]. The LC was well perfused throughout its thickness, with peak perfusion being slightly positioned towards its anterior region at 90 μm depth.

The AR-PAM system was used to assess the time-dependent perfusion state of the LC due to its greater penetration depth, which was required for imaging from the posterior of the ocular globe. Although a significant amount of resolution was sacrificed, the scan time was vastly reduced from 30 min in OR-PAM to 4 min in AR-PAM, allowing data acquisition at approximately 5–10 min intervals. An OR-PAM system using a Galvo or micro-electronic mechanical systems (MEMS) scanner (with a higher-repetition-rate excitation laser) can significantly improve the imaging speed [25,39]. A carbon contrast agent was also used for this purpose since it was particulate in nature and did not stain the LC's microcapillaries. The AR-PAM results (Fig. 5) show a change in perfusion state over 30 min, with an increasing trend from 5 to 20 min. Once the perfusion was stopped after 20 min, the signal intensity decreased significantly. From a quantitative analysis of a region of interest in Fig. 5(a), which was believed to be the region where the LC was located, the AR-PAM system was proved to be sensitive enough to detect changes in the perfusion state of the LC. Apart from the variation in intensity of the signal over time, new details also emerged in the image as the perfusion progressed, suggesting that more areas of the LC were perfused. Since the resolution of AR-PAM was limited at 45 μm, it was difficult to see the LC topography from the scanned images. Prior to the scan, we confirmed the location of the LC visually from the back of the ocular globe, as the LC region was visible after the optic nerve was cut short. This preliminary result shows that the AR-PAM system could show regional variations in blood flow, and the system was suitable for further quantitative analysis of the LC blood flow.

Fluorescence confocal microscopy is another alternative to assess LC perfusion. It is an established imaging modality that has found use in many fields including the perfusion of small capillaries both *in vivo* and *ex vivo*. For instance, Tomita *et al.* employed confocal fluorescence microscopy to study cortical microcirculation in murine to detect the local ischemic region [40]. In the aforementioned study, the scan area and depth (2 mm × 2 mm and 200 μm, respectively) were very close to the parameters used herein, barring the fact that the LC microcapillaries are significantly smaller and denser. However, confocal microscopy may not be able to capture the embedded capillaries of the LC. Also, depth information is an important parameter for LC perfusion, and photoacoustic detection may be more efficient than confocal microscopy, as confocal microscopy requires a shift in focal plane to acquire depth information.

Other optical techniques such as the laser Doppler flowmetry (LDF) and laser speckle flowgraphy (LSFG) have been used to study blood flow in the ONH [41,42]. LDF employs a laser to illuminate a small volume of tissue, and the backscattered light from moving red blood cells is collected to deduce flow velocity. However, LDF cannot provide blood flow data in an absolute unit, and spatial information is usually lost; hence, it is not suitable to observe blood variation in the LC. LSFG utilizes a high-resolution infrared charge-couple device (CCD) camera and an image analysis of speckle phenomenon to deduce a relative flow rate. It has been used in clinical settings to assess the blood flow in major arteries in the ONH *in vivo*. LSFG may also be another suitable technique for LC perfusion study, but the main downside is that it does not preserve depth information. Another technique is OCT angiography, which has been used to visualize the ONH microvasculature [43,44]. Whereas this technique offers excellent resolution, its penetration depth

is currently insufficient to visualize the LC in full, due to path obstruction by scattering in superficial ONH vessels, and quantification of blood flow has not yet been achieved.

Several limitations in our work warrant further discussion. The first limitation with the current experimental setup is the use of extrinsic contrast agents. In an ideal case, the best contrast agent to use is porcine blood; however, due to regulations, porcine blood was not available at the time of this study. The contrast agents used did not have the same osmolality and viscosity as natural blood, and this may affect tissue properties. Nevertheless, they were adequate for our purpose to obtain good photoacoustic imaging for demonstration purposes. Another limitation relates to the large variations in perfusion characteristics between each eye. For most eyes, the LC was not uniformly perfused, with the central area being more perfused than the periphery—this may or may not be representative of the physiological case. These variations impeded comparative studies among eyes. In addition, IOP was not controlled in this experiment, due to space constraints associated with the AR-PAM imaging system and the need of ocular dissection for OR-PAM imaging. Controlling IOP is crucial for investigative studies of factors that could affect the LC's perfusion state. Further work is thus required to improve on the current experimental setup.

There are also a few limitations with respect to the photoacoustic imaging system used in this study. It is currently unknown if the PAM signal scales linearly with blood flow, which is important if quantitative studies were to be conducted on LC perfusion. Another limitation is that even though the depth resolution of the OR-PAM allowed for some quantitative analysis of the perfusion profile along the LC depth, it was not sufficient to reconstruct a true three-dimensional vascular network, which required at least 4 µm resolution in all axes. Also, the current working distance (6.7 mm) and the limited penetration depth (∼1.4 mm) of the OR-PAM system did not allow for imaging of the LC from outside the ocular globe; these aspects may be improved with the use of both a longer focal length acoustic lens and low center frequency transducer to allow for perfusion monitoring with OR-PAM in the future. Also, an all-optical non-contact photoacoustic microscopy system will allow a true non-invasive imaging of the eye *in vivo* [45]. Lastly, the current OR-AR-PAM system could be further optimized to improve the scan time by modifying the system to acquire signal in both directions (instead of a single direction) or by using a MEMS scanning system and an optical scanning method.

It should also be noted that the current experimental setup was aimed to establish a means to study of LC perfusion *ex vivo*. While *in vivo* studies of the LC blood flow with an endogenous contrast agent (blood) should be the ultimate goal of PA imaging modality, it is still extremely challenging due to a relatively small and intricate network of the LC microcapillaries. Despite the fact that PA imaging has an advantage in penetration depth and is in theory more adept than other modalities in penetrating the deep structure in the ONH, no studies have yet revealed a detailed micro-vessel network in the ONH using PA imaging. *Ex vivo* images obtained from OR-PAM in this study retained defining characteristics of the LC, akin to LC images obtained from high-resolution *ex vivo* second harmonic imaging [46], while providing additional information on the LC's perfusion state. A lot has been learned about the biomechanical aspects of glaucoma from *ex vivo* study of glaucoma models in animals, but the current perspective is still lacking in hemodynamics aspects of the disease. The logical next step is to use the current setup to investigate the LC hemodynamics in the *ex vivo* animal models of glaucoma, specifically by varying the IOP and observing its effects on LC perfusion. In addition, various morphological (e.g., pore size, beam arrangement, connective tissue volume fraction) of the LC could be investigated to assess how they affect LC perfusion characteristics. Future works will also aim at adapting the current setup to image small rodents' LCs *in vivo*.

5. CONCLUSION

In conclusion, this work presents the first *ex vivo* experimental setup to study perfusion in LC microcapillaries using photoacoustic imaging. It was established that OR-PAM is a powerful imaging modality that can obtain high-resolution images of the LC, retaining the important morphological features while providing additional information on the perfusion state. The perfused OR-PAM images also verify an important notion that most of the LC collagen beams contain nourishing capillaries. AR-PAM was shown to be sensitive enough to detect time-dependent perfusion changes, which can be used in an investigation of various parameters associated with glaucoma, particularly the IOP, and how they can affect LC perfusion. The demonstration of LC PA imaging presented in this study is an important first step towards the elucidation of the important and unexplored hemodynamics aspect of the pathogenesis of glaucoma.

†These authors contributed equally to this work.

REFERENCES

1. R. N. Weinreb, T. Aung, and F. A. Medeiros, "The pathophysiology and treatment of glaucoma: a review," J. Am. Med. Assoc. **311**, 1901–1911 (2014).
2. A. J. Feola, B. Coudrillier, J. Mulvihill, D. M. Geraldes, N. T. Vo, J. Albon, R. L. Abel, B. C. Samuels, and C. R. Ethier, "Deformation of the lamina cribrosa and optic nerve due to changes in cerebrospinal fluid pressure," Invest. Ophthalmol. Visual Sci. **58**, 2070–2078 (2017).
3. X. F. Wang, L. K. Fisher, D. Milea, J. B. Jonas, and M. J. A. Girard, "Predictions of optic nerve traction forces and peripapillary tissue stresses following horizontal eye movements," Invest. Ophthalmol. Visual Sci. **58**, 2044–2053 (2017).
4. N. G. Strouthidis and M. J. Girard, "Altering the way the optic nerve head responds to intraocular pressure-a potential approach to glaucoma therapy," Curr. Opin. Pharmacol. **13**, 83–89 (2013).
5. C. F. Burgoyne, J. C. Downs, A. J. Bellezza, J. K. Suh, and R. T. Hart, "The optic nerve head as a biomechanical structure: a new paradigm for understanding the role of IOP-related stress and strain in the pathophysiology of glaucomatous optic nerve head damage," Prog. Retinal Eye Res. **24**, 39–73 (2005).
6. H. A. Quigley, S. J. McKinnon, D. J. Zack, M. E. Pease, L. A. Kerrigan-Baumrind, D. F. Kerrigan, and R. S. Mitchell, "Retrograde axonal

transport of BDNF in retinal ganglion cells is blocked by acute IOP elevation in rats," Invest. Ophthalmol. Visual Sci. **41**, 3460–3466 (2000).

7. T. Chuangsuwanich, K. E. Birgersson, A. Thiery, S. G. Thakku, H. L. Leo, and M. J. A. Girard, "Factors influencing lamina cribrosa microcapillary hemodynamics and oxygen concentrationsmodeling of lamina cribrosa hemodynamics," Invest. Ophthalmol. Visual Sci. **57**, 6167–6179 (2016).

8. T. Nakazawa, "Ocular blood flow and influencing factors for glaucoma," Asia-Pac. J. Ophthalmol. **5**, 38–44 (2016).

9. V. P. Costa, A. Harris, D. Anderson, R. Stodtmeister, F. Cremasco, H. Kergoat, J. Lovasik, I. Stalmans, O. Zeitz, I. Lanzl, K. Gugleta, and L. Schmetterer, "Ocular perfusion pressure in glaucoma," Acta Ophthalmol. (Copenh.) **92**, e252–e266 (2014).

10. A. P. Cherecheanu, G. Garhofer, D. Schmidl, R. Werkmeister, and L. Schmetterer, "Ocular perfusion pressure and ocular blood flow in glaucoma," Curr. Opin. Pharmacol. **13**, 36–42 (2013).

11. C. F. Burgoyne, "A biomechanical paradigm for axonal insult within the optic nerve head in aging and glaucoma," Exp. Eye Res. **93**, 120–132 (2011).

12. V. Ntziachristos, "Going deeper than microscopy: the optical imaging frontier in biology," Nat. Methods **7**, 603–614 (2010).

13. P. K. Upputuri and M. Pramanik, "Recent advances toward preclinical and clinical translation of photoacoustic tomography: a review," J. Biomed. Opt. **22**, 041006 (2017).

14. L. V. Wang and J. Yao, "A practical guide to photoacoustic tomography in the life sciences," Nat. Methods **13**, 627–638 (2016).

15. Y. Zhou, J. Yao, and L. V. Wang, "Tutorial on photoacoustic tomography," J. Biomed. Opt. **21**, 061007 (2016).

16. A. Taruttis and V. Ntziachristos, "Advances in real-time multispectral optoacoustic imaging and its applications," Nat. Photonics **9**, 219–227 (2015).

17. P. K. Upputuri and M. Pramanik, "Dynamic in vivo imaging of small animal brain using pulsed laser diode-based photoacoustic tomography system," J. Biomed. Opt. **22**, 090501 (2017).

18. J. Yao, A. A. Kaberniuk, L. Li, D. M. Shcherbakova, R. Zhang, L. Wang, G. Li, V. V. Verkhusha, and L. V. Wang, "Multiscale photoacoustic tomography using reversibly switchable bacterial phytochrome as a near-infrared photochromic probe," Nat. Methods **13**, 67–73 (2016).

19. W. Liu and H. F. Zhang, "Photoacoustic imaging of the eye: a mini review," Photoacoustics **4**, 112–123 (2016).

20. D. Pan, M. Pramanik, A. Senpan, J. S. Allen, H. Zhang, S. A. Wickline, L. V. Wang, and G. M. Lanza, "Molecular photoacoustic imaging of angiogenesis with integrin-targeted gold nanobeacons," FASEB J. **25**, 875–882 (2011).

21. M. Moothanchery and M. Pramanik, "Performance characterization of a switchable acoustic and optical resolution photoacoustic microscopy system," Sensors **17**, 357 (2017).

22. M. Moothanchery, R. Z. Seeni, C. Xu, and M. Pramanik, "In vivo studies of transdermal nanoparticle delivery with microneedles using photoacoustic microscopy," Biomed. Opt. Express **8**, 5483–5492 (2017).

23. S. Park, C. Lee, J. Kim, and C. Kim, "Acoustic resolution photoacoustic microscopy," Biomed. Eng. Lett. **4**, 213–222 (2014).

24. H. F. Zhang, K. Maslov, G. Stoica, and L. V. Wang, "Functional photoacoustic microscopy for high-resolution and noninvasive in vivo imaging," Nat. Biotechnol. **24**, 848–851 (2006).

25. J. Y. Kim, C. Lee, K. Park, G. Lim, and C. Kim, "Fast optical-resolution photoacoustic microscopy using a 2-axis water-proofing MEMS scanner," Sci. Rep. **5**, 7932 (2015).

26. P. Hai, J. Yao, K. I. Maslov, Y. Zhou, and L. V. Wang, "Near-infrared optical-resolution photoacoustic microscopy," Opt. Lett. **39**, 5192–5195 (2014).

27. C. Zhang, K. Maslov, S. Hu, R. Chen, Q. Zhou, K. K. Shung, and L. V. Wang, "Reflection-mode submicron-resolution in vivo photoacoustic microscopy," J. Biomed. Opt. **17**, 020501 (2012).

28. W. Song, Q. Wei, W. Liu, T. Liu, J. Yi, N. Sheibani, A. A. Fawzi, R. A. Linsenmeier, S. Jiao, and H. F. Zhang, "A combined method

to quantify the retinal metabolic rate of oxygen using photoacoustic ophthalmoscopy and optical coherence tomography," Sci. Rep. **4**, 6525 (2014).

29. W. Song, Q. Wei, T. Liu, D. Kuai, J. M. Burke, S. L. Jiao, and H. F. Zhang, "Integrating photoacoustic ophthalmoscopy with scanning laser ophthalmoscopy, optical coherence tomography, and fluorescein angiography for a multimodal retinal imaging platform," J. Biomed. Opt. **17**, 061206 (2012).

30. S. Hu, B. Rao, K. Maslov, and L. V. Wang, "Label-free photoacoustic ophthalmic angiography," Opt. Lett. **35**, 1–3 (2010).

31. A. de la Zerda, Y. M. Paulus, R. Teed, S. Bodapati, Y. Dollberg, B. T. Khuri-Yakub, M. S. Blumenkranz, D. M. Moshfeghi, and S. S. Gambhir, "Photoacoustic ocular imaging," Opt. Lett. **35**, 270–272 (2010).

32. S. Jeon, H. B. Song, J. Kim, B. J. Lee, R. Managuli, J. H. Kim, J. H. Kim, and C. Kim, "In vivo photoacoustic imaging of anterior ocular vasculature: a random sample consensus approach," Sci. Rep. **7**, 4318 (2017).

33. M. Moothanchery, A. Sharma, and M. Pramanik, "Switchable acoustic and optical resolution photoacoustic microscopy for in vivo small-animal blood vasculature imaging," J. Visualized Exp. **124**, e55810 (2017).

34. B. Coudrillier, D. M. Geraldes, N. T. Vo, R. Atwood, C. Reinhard, I. C. Campbell, Y. Raji, J. Albon, R. L. Abel, and C. R. Ethier, "Phase-contrast micro-computed tomography measurements of the intraocular pressure-induced deformation of the porcine lamina cribrosa," IEEE Trans. Med. Imaging **35**, 988–999 (2016).

35. C. W. Spraul, G. E. Lang, and H. E. Grossniklaus, "Morphometric analysis of the choroid, Bruch's membrane, and retinal pigment epithelium in eyes with age-related macular degeneration," Invest. Ophthalmol. Visual Sci. **37**, 2724–2735 (1996).

36. P. Causin, G. Guidoboni, A. Harris, D. Prada, R. Sacco, and S. Terragni, "A poroelastic model for the perfusion of the lamina cribrosa in the optic nerve head," Math. Biosci. **257**, 33–41 (2014).

37. T.-W. Kim, L. Kagemann, M. J. A. Girard, N. G. Strouthidis, K. R. Sung, C. K. Leung, J. S. Schuman, and G. Wollstein, "Imaging of the lamina cribrosa in glaucoma: perspectives of pathogenesis and clinical applications," Curr. Eye Res. **38**, 903–909 (2013).

38. N. Fatehee, P. K. Yu, W. H. Morgan, S. J. Cringle, and D. Y. Yu, "Correlating morphometric parameters of the porcine optic nerve head in spectral domain optical coherence tomography with histological sections," Br. J. Ophthalmol. **95**, 585–589 (2011).

39. B. Ning, N. Sun, R. Cao, R. Chen, K. Kirk Shung, J. A. Hossack, J. M. Lee, Q. Zhou, and S. Hu, "Ultrasound-aided multi-parametric photoacoustic microscopy of the mouse brain," Sci. Rep. **5**, 18775 (2015).

40. Y. Tomita, N. Kubis, Y. Calando, A. T. Dinh, P. Méric, J. Seylaz, and E. Pinard, "Long-term in vivo investigation of mouse cerebral microcirculation by fluorescence confocal microscopy in the area of focal ischemia," J. Cereb. Blood Flow Metab. **25**, 858–867 (2005).

41. C. E. Riva, M. Geiser, and B. L. Petrig, "Ocular blood flow assessment using continuous laser Doppler flowmetry," Acta Ophthalmol. (Copenh.) **88**, 622–629 (2010).

42. T. Sugiyama, M. Araie, C. E. Riva, L. Schmetterer, and S. Orgul, "Use of laser speckle flowgraphy in ocular blood flow research," Acta Ophthalmol. (Copenh.) **88**, 723–729 (2010).

43. C. L. Chen and R. K. Wang, "Optical coherence tomography based angiography," Biomed. Opt. Express **8**, 1056–1082 (2017).

44. R. A. Leitgeb, R. M. Werkmeister, C. Blatter, and L. Schmetterer, "Doppler optical coherence tomography," Prog. Retin. Eye Res. **41**, 26–43 (2014).

45. P. Hajireza, W. Shi, K. Bell, R. J. Paproski, and R. J. Zemp, "Non-interferometric photoacoustic remote sensing microscopy," Light Sci. Appl. **6**, e16278 (2017).

46. D. J. Brown, N. Morishige, A. Neekhra, D. S. Minckler, and J. V. Jester, "Application of second harmonic imaging microscopy to assess structural changes in optic nerve head structure ex vivo," J. Biomed. Opt. **12**, 024029 (2007).